Research Square

Preprints are preliminary reports that have not undergone peer review.
They should not be considered conclusive, used to inform clinical practice,
or referenced by the media as validated information.

Monitoring Lithiation Gradients in Solid-state Batteries Using Operando Neutron Radiography

Patrice Perrenot

pperrenot@gmail.com

LEPMI

Lukas Helfen

Institut Laue Langevin (ILL)

Ove Korjus

https://orcid.org/0000-0003-2151-0440

Oskar Thompson

LEPMI - CNRS - UGA

Fannie Alloin

LEPMI - CNRS - UGA https://orcid.org/0000-0001-7882-1587

Claire Villevieille

LEPMI https://orcid.org/0000-0001-8782-4800

Article

Keywords:

Posted Date: June 5th, 2026

DOI: https://doi.org/10.21203/rs.3.rs-9486004/v1

License: This work is licensed under a Creative Commons Attribution 4.0 International License.
Read Full License

Additional Declarations: There is **NO** Competing Interest.

Monitoring Lithiation Gradients in Solid-state Batteries Using *Operando* Neutron Radiography

Patrice Perrenot[1], Lukas Helfen[2], Ove Korjus[2], Oskar Thompson[1], Fannie Alloin[1], Claire Villevieille[1]**

1. *Univ. Grenoble Alpes, Univ. Savoie Mont Blanc, CNRS, Grenoble INP, LEPMI, 38000 Grenoble, France*
2. *Institut Laue-Langevin, 71 Avenue des Martyrs, 38000 Grenoble, France*

Corresponding Author

* E-mail: patrice.perrenot@grenoble-inp.fr; claire.villevieille@grenoble-inp.fr

1. Abstract

Monitoring local lithium-ion transport is crucial to the design of high-performance, high-loading composite electrodes for next-generation solid-state batteries. Nowadays, this transport is determined either globally by averaging whole-cell properties or indirectly using advanced, tedious characterization techniques. Here, we directly visualize lithium-ion transport in a solid-state battery comprising a composite positive electrode made of Li_6PS_5Cl (LPSCl) and $LiNi_{0.5}Mn_{0.3}Co_{0.2}O_2$ (NMC532), a LPSCl separator, and an ^{6}Li-In negative electrode. Exploiting the isotopic sensitivity of neutron radiography and the high spatial resolution offered by NeXT beamline (ILL), we monitor lithium gradients across both the separator and the composite electrode during cycling. This paper demonstrates that the lithium gradients emerge from both the electrochemical migration and the isotopic diffusion, a transport phenomenon often overlooked during neutron experiments. Spatially-resolved analysis reveals enhanced lithium transport when densification is optimized. However, the edge effect is also playing a role in solid-state batteries with weaker densification, thus impacting the current density distribution. These densification disparities induce heterogeneous Li-ion transport across the cell.

2. Introduction

Solid-state batteries are considered to represent the next generation of electrochemical energy systems, due to their enhanced safety and high energy density[1–3]. Among the existing family of solid electrolytes, thiophosphate-based electrolytes have several advantages, including low cost, ease of processing at room temperature, low density, and compatibility with industrial-scale up[4–8]. However, these advantages have yet to be achieved due to the current lack of control over the interfaces, particularly in the composite electrode. Efficient transport of lithium ions is mandatory at the interfaces between solid components, to ensure short percolation pathways for both ions and electrons throughout the cell[9]. This is a critical parameter, especially in solid-state batteries, since high-load positive composite electrodes are needed to reach high energy density[10–12]. Thus, good ionic and electronic transports within a composite electrode are of utmost importance, but the understanding has been restricted due to the lack of characterization techniques.

As discussed, achieving theoptimal morphology of composite electrodes remains a challenge[13] because i) the electroactive materials can fracture during densification[14,15], ii) a residual porosity is always present within the composite electrode[16–18], iii) the interfacial contacts between the electroactive materials and the solid electrolyte are not optimal, and iv) when an optimal contact is reached, generally it leads to interfacial decomposition reducing the transport/transfer of Li-ions[19]. Therefore, monitoring the Li-ion transport properties during cycling of a thick composite electrode is of paramount importance for tracking the weakness of the electrode manufacturing. To date, lithium-ion transport has been assessed through global and sample-averaged measurements[17,20,21] (e.g., electrochemical techniques, X-ray diffraction, X-ray absorption spectroscopy) or through highly localized surface-sensitive techniques[22] (e.g., TOF-SIMS measurement). In addition, the ion pathways are typically deduced from 3D imaging

reconstructions, meaning that spatial bottlenecks and anisotropic conduction within the ion-conducting phase remain poorly quantified.

Several groups have investigated the Li-ion transport by observing a gradient in solid-state batteries using thick electrodes. Davis *et al.* used *operando* microscopy to track heterogeneity at the interface between Li_6PS_5Cl (LPSCl) and the graphite electrode[23]. They demonstrated that heterogeneities are linked to electrode microstructure and poor ionic transport within the solid electrolyte at high C-rate. Nevertheless, such *operando* microscopy only tracks the heterogeneity at the surface of the composite electrode, and concerns could arise when extending observation to the bulk of the electrode. Stavola *et al.* investigated the lithiation gradient in the thick composite electrode of NMC111 using high-resolution X-ray diffraction at large-scale facilities[24]. They found a current distribution within the electrode volume already at a C/10 rate, showing the difficult Li-ion transport in a 110 µm thick electrode. This technique analyzes the entire depth of the sample; however, the lithium concentrations are indirectly calculated from the active materials structure, and therefore neglect the lithium transport through the electrolyte, resulting in only a partial view of the ionic transport. Moreover, the signal is averaged over approximately 20 µm, which can obscure local phenomena and spatial heterogeneities.

Due to the lithium 6-isotope's high sensitivity, neutron imaging could become a game changer when it comes to the determination of the lithium-ion transport in batteries[25–29]. Bradbury *et al.* investigated an all-solid-state Li-S battery by *operando* neutron radiography and tomography using the lithium isotope contrast[30]. They visualized the lithium transport in a solid-state battery, but with a rather low spatial resolution (13 µm), meaning that the limitation in the transport mechanisms could not be properly deduced. Moreover, the acquisition of the tomographic volume was time-consuming, requiring the battery to be paused during imaging, leading to

biased results since the cell would re-equilibrate and mitigate the dynamics of Li-ions. Recent advancements in neutron radiography have enhanced spatial resolution to 7.5 µm, enabling more accurate characterization [31]. These neutron-based imaging studies have primarily focused on the central region of the cell, thereby overlooking edge effects inherent to cylindrical geometries. Critically, observations of lithium accumulation within the separator, occurring during charge in opposition to the expected electrochemical migration, remain unaddressed.

In this work, we monitor the Li-ion transport within a solid-state battery comprising NMC532 as active material and LPSCl as solid electrolyte using *operando* neutron radiography and a ^{6}Li isotope-enriched indium metal negative electrode. A dedicated setup has been designed to allow *operando* imaging under stack pressure with an improved spatial discretization of 2.65 µm. Thanks to a careful investigation, we highlight simultaneous transport phenomena, the isotopic diffusion and the electrochemical migration, and their relative contribution during charge and discharge. Moreover, we link the lithium transport to morphological features from uniaxially densified solid-state batteries.

3. Results

In this article, multiple terminologies will be used to describe the lithium transport and separate the contribution of each lithium isotope. Indeed, neutron imaging is sensitive to ^{6}Li, and not to ^{7}Li due to their different neutron attenuation coefficient (78.313 vs 0.067 cm^{-1}, respectively). However, those isotopes are never found in their pure form. Hence, the lithium foil used for producing the battery is enriched in ^{6}Li to 95%, the rest being ^{7}Li. In opposition, the natural isotopic abundance of Li, written ^{nat}Li, only contains 7.4% of ^{6}Li (such as LPSCl and NMC used in this cell) and possesses a neutron attenuation coefficient of 5.150 cm^{-1}. In the latter, we will refer to ^{6}Li, the isotope that we can track and measure, while ^{7}Li is the isotope that can be deduced. When the transport of both isotopes is discussed, the Li term will be used.

3.1. Observations prior to cycling

A neutron radiograph, obtained after a first charge performed in the laboratory (to start the neutron measurement with a delithiated NMC electrode), in **Figure 1a** highlights the different cell components. The setup is further presented in **Figure S1** in **Supplementary Information**. The images are normalized by the sample thickness at each pixel, allowing us to get an equivalent ^{6}Li atomic density. The cycling curve during the neutron experiment is presented in **Figure 1b**.

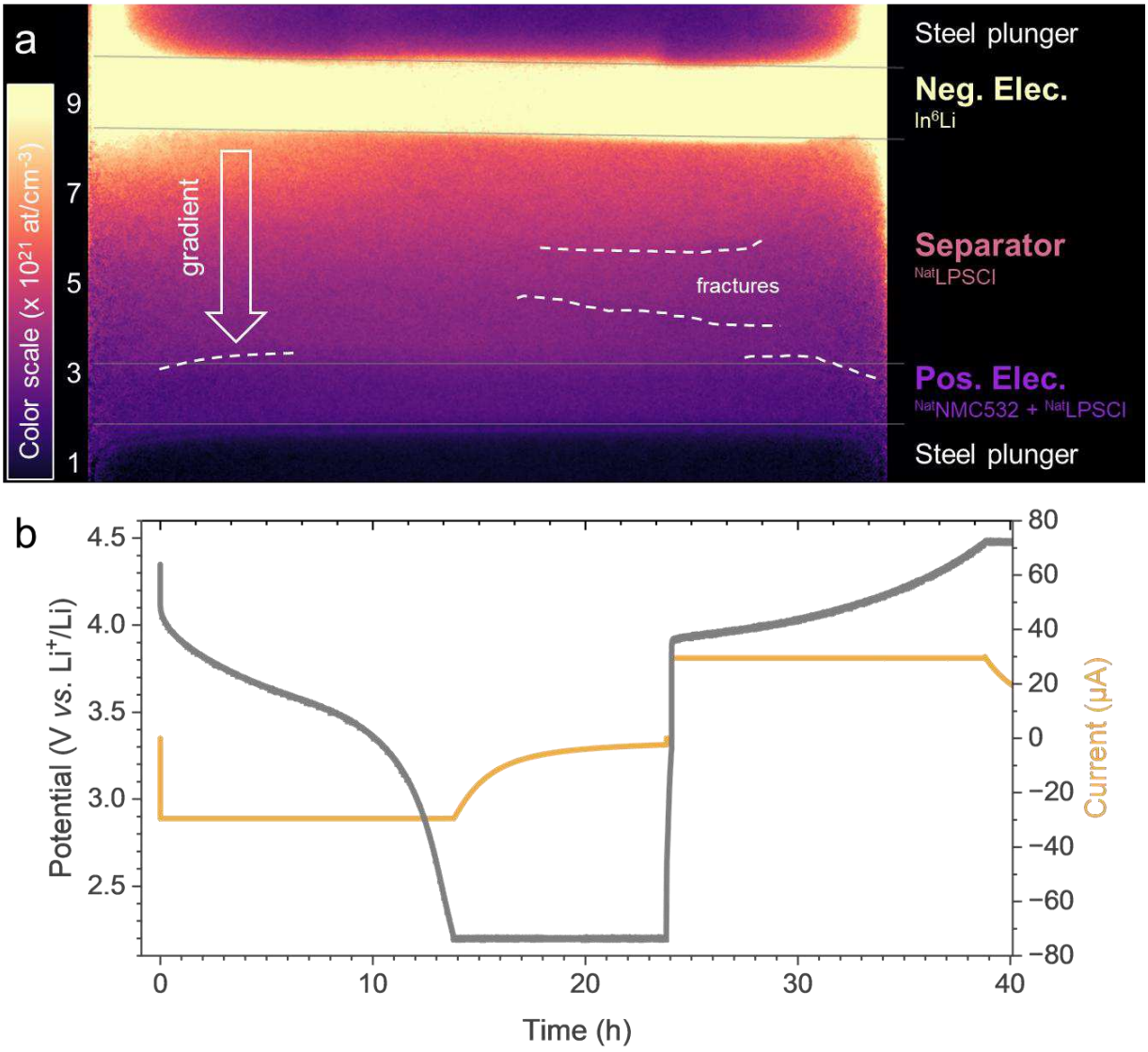


Figure 1: **Operando neutron radiography and electrochemical profile of a solid-state cell after initial charge.** a) Neutron radiography highlighting the different cell components obtained after the first charge. The gradient of color (big arrow), as well as the fractures (dashed lines) in the separator, are highlighted. The arrow represents the gradient in the direction of the spontaneous isotopic diffusion of ^{6}Li from high concentration in orange to low concentration in violet, and b) Electrochemical profile of the cell cycled in CCCV (Constant Current Constant Voltage) mode at a C/20 rate between 4.5 and 2.2 V vs Li^{+}/Li at the NeXT instrument.

OCV neutron radiograph after the first charge reveals several microstructural features as well as isotopic diffusion (**Figure 1a**). First, a ^{6}Li gradient across the separator (arrow in **Figure 1a**, from approx. 7 to 3 x10^{21} at/cm^{3}) indicates spontaneous isotopic diffusion from the ^{6}Li-In negative electrode into the ^{nat}LPSCl separator, a process discussed in detail in the following section (Isotopic diffusion vs. electrochemical migration**)**.

From a microstructure point-of-view, four fractures can be seen in the separator and at the positive electrode/separator interface (**Figure 1a**, dashed white lines). Given that radiography provides only a two-dimensional projection, precise quantification of fracture dimensions and the three-dimensional Li pathway remains challenging. However, these defects, oriented perpendicular to the primary Li-ion transport direction, are likely to locally hinder ionic conduction during cycling.

Finally, as the electrode was first delithiated in the laboratory, we notice a slight contrast between the positive electrode and the separator that further supports efficient electrochemical delithiation of NMC, despite the high electrode loading (**Figure S2, Supplementary Information**). This contrast is further supported by the experimental calculation of ^{6}Li in the separator and the positive electrode at the charged state (2.0 x10^{21} vs 1.52 x10^{21} at/cm^{3}, respectively).

3.2. *Operando* monitoring of the positive electrode and separator during cycling

During the first discharge and the second charge (**Figure 1b**), it is possible to monitor *operando* the dynamics of ^{6}Li transport through the evolution of the neutron radiography (**Figure 2**). To avoid confusion during discussion, the term Depth of Discharge (DoD) will be used during the first discharge, while State of Charge (SoC) will be used during the second charge. We consider that the state at the end of the discharge is equivalent to the state at the start of the

subsequent charge; in other terms, a DoD of 100% is equivalent to a SoC of 0%. A movie is available to visualize the Li transport dynamics in the **Supplementary Information (Movie 1)**.

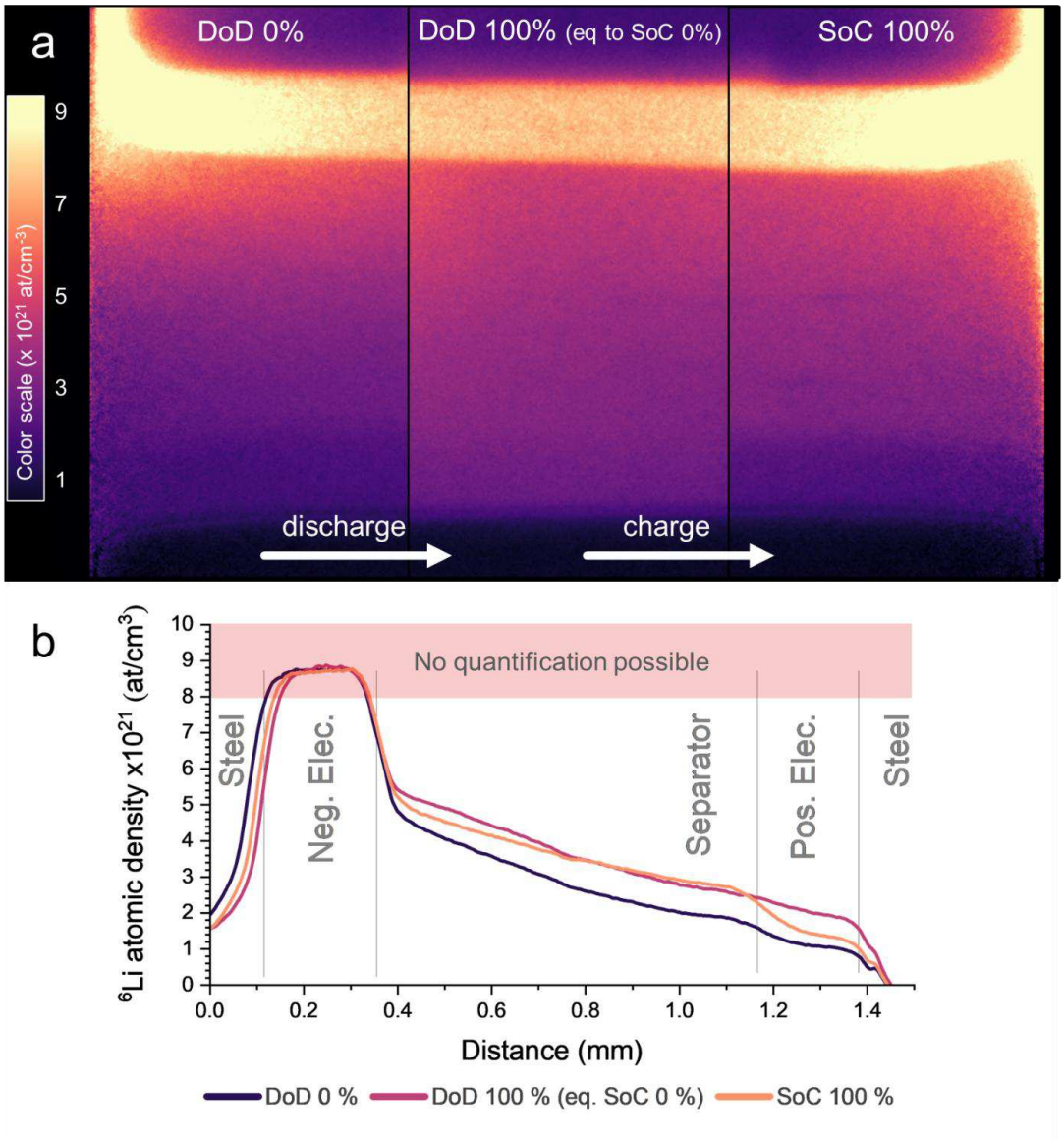


Figure 2: ***Operando*** **neutron radiography of ^{6}Li redistribution during cycling at key states of discharge and charge.** a) Neutron radiography images at DoD 0 % (left), at DoD 100 %, equivalent to SoC 100 % (center), and at SoC 100 % (right), and b) their associated ^{6}Li concentration profiles that highlight the evolution of Li-ion concentration during cycling.

From **Figure 2**, the positive electrode effectively gains ^{6}Li during the discharge (NMC lithiation) and loses them back during the following charge (NMC delithiation). Furthermore, an

irreversible enrichment of ^{6}Li develops within the separator, consistent with continuous isotopic diffusion from the ^{6}Li-In negative electrode toward the positive electrode (**Movie 1**). Contrary to the negative electrode, which is dominated by the ^{6}Li total absorption, making ^{6}Li quantification impossible, the separator and the positive electrode are not fully enriched in ^{6}Li but are made of a mixture of ^{6}Li and ^{7}Li, with a ratio evolving with time. This spatially heterogeneous distribution arises from both electrochemical migration and isotopic diffusion, which together govern the observed lithium transport dynamics throughout the solid-state cell.

3.3. Isotopic diffusion vs. electrochemical migration

3.3.1. Isotopic diffusion

From the cell manufacturing, the difference in isotope concentration between the ^{6}Li-In negative electrode and the ^{nat}LPSCl separator (95% ^{6}Li-5% ^{7}Li and 7.4% ^{6}Li-92.6% ^{7}Li, respectively) will lead to an isotope diffusion from the higher concentration region to the lower concentration region, a so-called isotopic diffusion process. We calculate the expected ^{6}Li concentration in the different cell components at fabrication time and after infinite diffusion time, considering that all lithium-ion in LPSCl can be exchanged from ^{nat}Li to ^{6}Li, using the weight of each component (**Figure 3a**). The calculations to support **Figure 3** are available in **Table 1**. Calculations details are found in **Supplementary Information** in **Note S1.** Concentration calculations alongside **Figure S3.** The isotopic diffusion is schematized in **Figure 3d**.

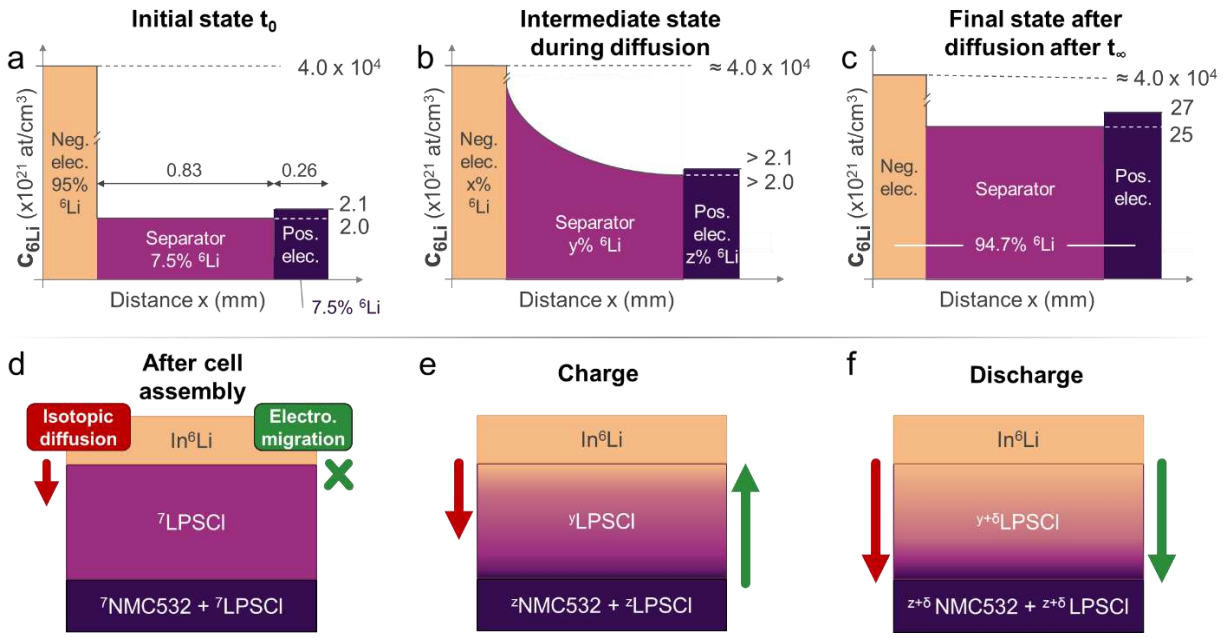


Figure 3: **Simulated ^{6}Li atomic density profiles at key stages** (based on calculation from cell fabrication without electrochemical migration): a) initial cell assembly, b) intermediate diffusion, and c) infinite diffusion time, illustrating the interplay of isotopic diffusion and electrochemical migration (red and green arrows, respectively) during d) assembly, e) charge, and f) discharge.

Table 1: Concentration calculation at the initial state t_0 and at infinite time. The bold values are the ones presented in **Figure 3**.

Metrics in pristine state	**Composite positive electrode**	**Separator**	**Negative electrode**
Initial state before diffusion			
Li amount of substance $n_{Li\ tot}$ (mol)	$7.51\ 10^{-5}$	$2.59\ 10^{-4}$	$1.25\ 10^{-1}$
^{6}Li amount of substance n_{6Li} (mol)	$5.71\ 10^{-6}$	$1.97\ 10^{-5}$	$1.18\ 10^{-1}$
^{7}Li amount of substance n_{7Li} (mol)	$6.94\ 10^{-5}$	$2.40\ 10^{-4}$	$6.23\ 10^{-3}$
Percentage of ^{6}Li (%)	**7.6**	**7.6**	**95**

^{6}Li concentration at initial state $C_{6Li\ t0}$ (at/cm^3)	**2.15 10^{21}**	**2.02 10^{21}**	**3.95 10^{25}**
^{7}Li concentration at initial state $C_{7Li\ t0}$ (at/cm^3)	2.61 10^{22}	2.46 10^{22}	2.08 10^{24}
Final state after infinite time diffusion			
^{6}Li amount of substance after infinite diffusion $n_{6Li\ inf\ diff}$ (mol)	7.12 10^{-5}	2.46 10^{-4}	1.18 10^{-1}
^{7}Li amount of substance after infinite diffusion $n_{7Li\ inf\ diff}$ (mol)	3.93 10^{-6}	1.36 10^{-5}	6.52 10^{-3}
^{6}Li concentration after infinite diffusion $C_{6Li\ inf\ diff}$ (at/cm^3)	**2.68 10^{22}**	**2.52 10^{22}**	**3.94 10^{25}**
^{7}Li concentration after infinite diffusion $C_{7Li\ inf\ diff}$ (at/cm^3)	1.48 10^{21}	1.39 10^{21}	2.18 10^{24}
Global percentage of ^{6}Li (%)		**94.77**	

From these observations, several key insights emerge. First, the amount of ^{6}Li originating from the negative electrode vastly exceeds the ^{6}Li content within the rest of the cell (4.0×10^{25} versus 5.6×10^{21} atoms, respectively), effectively constituting an infinite isotopic reservoir. Over sufficiently long timescales, the isotope gradient of concentration between ^{6}Li and ^{7}Li will no longer exist, driving each component toward the overall isotopic equilibrium of 94.7% ^{6}Li (**Figure 3c**). Considering its ^{6}Li content, the negative electrode serves as a constant source. Because the solid phases in the battery do not constitute a dilute solution, Fick's second law of diffusion cannot strictly be applied.

3.3.2. Electrochemical migration

When the current is applied, Li-ions migrate from one electrode to the other (green arrows in **Figure 3e, f**). The number of Li-ions moving will depend on the total charges exchanged during

the discharging/charging process, and its velocity will depend on the effective ionic conductivity of the materials (taking into account the tortuosity path). Considering the high coulombic efficiency between the discharge and the subsequent charge (98.3%), meaning that parasite reactions are considered negligible, it is assumed that the charges exchanged during cycling will strictly induce the transport of Li^+, consistent with the behavior of LPSCl as a Li^+ unipolar conductor.

Now, when examining and quantifying Li-ions in the cell, we need to remember that during the charge, electrochemical migration and isotopic diffusion will be in opposite directions, while during discharge, they will share the same direction (**Figure 3e, 3f**).

3.4. Deciphering between isotopic diffusion and electrochemical migration

Both phenomena happened to the cell before the beginning of the neutron imaging experiment, first during the cell assembly (spontaneous isotopic diffusion) and second during the first charge (spontaneous isotopic diffusion and electrochemical migration). The cell has been manufactured and directly charged for 38 h and 39 min (**Figure S2**), starting both the electrochemical migration from the positive electrode to the negative electrode and the isotopic diffusion from the negative to the positive electrode. The cell has then been brought to the beam, and approximately 18 h have passed before starting the experiment (due to transport, beam alignment, etc.), where isotopic diffusion has continued (exchange of ^6Li and ^7Li). Prior starting the measurement, the cell was on potential hold up to 4.5 V vs. Li^+/Li during the beam alignment to compensate for the ohmic drop that occurred during the transport from laboratory to the beam. To disentangle the distinct phenomena occurring during the discharge and the charge, the evolution of the average ^6Li concentration along the different cell components can be plotted at various DoD and SoC, respectively. However, as commonly observed in solid state batteries, it is important to separate the cell edges from the center (**Movie 1, Supplementary information**)

since the densification is never homogeneous. To elucidate the underlying transport mechanisms, we therefore analyze the edge and center regions independently. While full-width profiles are provided in **Figure S4**, we first focus on the center of the cell which is more representative of a solid-state battery (**Figure 4**).

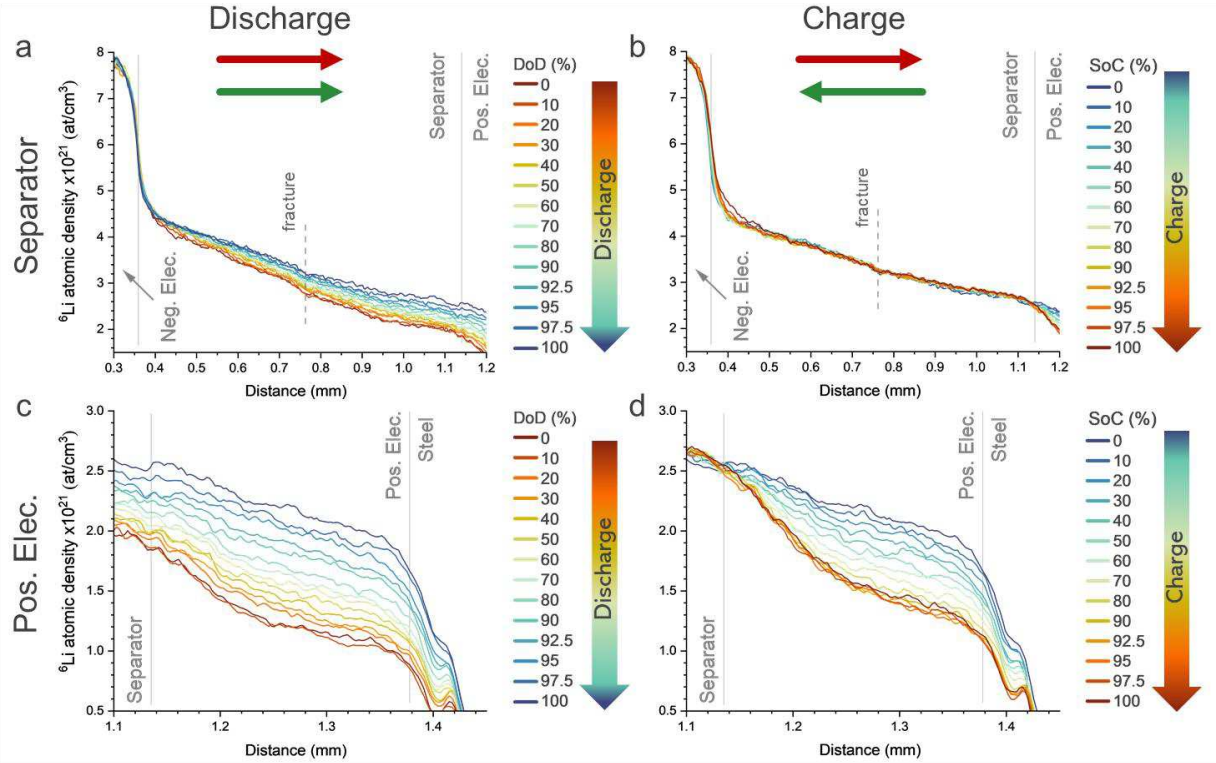


Figure 4: **Evolution of ^{6}Li content during cycling at the center of the cell.** Profiles of ^{6}Li content along the cell components at different DoD and SoC during a, c) discharge and b, d) charge, averaged over a width of 265 µm in the center of the cell. The top panels focus on the separator, and the bottom panels focus on the positive electrode, respectively. The top red and green arrows highlight the direction of the isotopic diffusion and the electrochemical migration, respectively. The dashed line indicates the position of an identified fracture. The right arrows help visualize the curves' evolution during cycling with the same color code as the curves.

3.4.1. Lithium transport of the LPSCl separator (center of the cell)

The initial ^{6}Li gradient at the onset of the experiment led to an average ^{6}Li concentration in the separator that nearly doubled at the negative/electrolyte interface compared to its initial state (2.02 10^{21} at/cm3, **Table 1**), whereas the ^{6}Li concentration at the electrolyte/positive electrode is close to the initial concentration (approx. 4.0 x10^{21} at/cm^{3} and 1.95 x10^{21} at/cm^{3}, respectively). The total duration of the *operando* measurement is insufficient for achieving infinite time isotopic exchange over the full thickness of the cell (**Figure 2b**, extended representation in **Figure S4**), implying that diffusion and migration coexist and superimpose during cycling, alongside localized effects.

During discharge (lithiation of NMC), a continuous increase in ^{6}Li content was observed within the LPSCl separator (**Figure 4a**), with a more noticeable effect on the positive electrode side. This increase aligns with expectations, given the substantial ^{6}Li reservoir at the negative electrode and the strong isotopic gradient between the negative electrode and the separator initial state (95% ^{6}Li versus 7.6%, respectively). In addition to the electrochemical migration process, this establishes a pronounced isotopic chemical potential gradient, varying across the separator, that should drive ^{6}Li redistribution. Importantly, not all lithium species within the LPSCl participate equally in the exchange process: only a fraction of Li, likely those contributing to ionic conductivity in the argyrodite lattice, are effectively mobile on the timescale of the experiment[32]. As a result, the measured ^{6}Li enrichment remains far from the infinite-time isotopic equilibrium value (approx. 25 x10^{21} at/cm^{3}). This evolution of ^{6}Li content does not strictly scale linearly with DoD over the whole discharge. Instead, the ^{6}Li concentration evolved more linearly as a function of DoD during constant current (CC), while it evolved more linearly as a function of the square root of time during constant voltage (CV), suggesting a coupled transport mechanism in the separator (**Figure S5**). The relative contribution of these two

transport mechanisms varies as the migration decreases during the CV, with the current, resulting in a non-linear temporal evolution of ^{6}Li content.

Upon charging (**Figure 4b**), the behavior diverges sharply from that observed on discharge: with almost no evolution of ^{6}Li concentration in all the electrolyte thickness, isotopic diffusion and migration proceed in opposite directions and counterbalance one another reaching a near-equilibrium state. The stationary state observed allows us to determine the isotopic diffusion coefficient, given the known migration flux. Following the methodology described in **Note S2.** Quasi-stationary state of transport during charging through the separator in **Supplementary Information**, the diffusion coefficient of ^{6}Li through LPSCl separator is calculated at 2.4 x10^{-6} cm²/s. This value aligns well with literature reports [33].

3.4.2. Lithium transport in the composite positive electrode (center of the cell)

During the discharge, a progressive increase in ^{6}Li concentration is observed within the positive electrode, consistent with lithium insertion into NMC particles (**Figure 4c**), with a gradient from the separator surface to the current collector side, the ^{6}Li content being higher at the separator side. The gradient transition between the separator and the positive electrode (from 1.1 to 1.25 mm) is attributed to the slight tilt of the cell compared to the beam axis (estimated at 2.9°), as well as a rough electrolyte/electrode interface due to the piston rugosity (used in successive densification), aligned with observations reported in a previous solid-state study[34]. Indeed, a thickness of 150 µm transition is seen to go from the separator behavior (1.1 mm) to the positive electrode (1.25 mm). At the beginning of the discharge (0% DoD, **Figure 4c**), past 1.25 mm, a ^{6}Li quasi-constant concentration, lower than the calculated one, is observed (1.15x10^{21} at/cm^{3} instead of 1.5x10^{21} at/cm^{3}, **Table S2**). This difference may be associated with the porosity of the electrode (estimated from the ^{6}Li atomic concentration difference at approx. 23 %) and poor isotopic diffusion in the electrode before discharge (due to time, distances from

the negative to the positive electrode and the tortuosity). Past 1.25 mm (half of the positive electrode on the current collector side), in addition to NMC lithiation, the increase in ^{6}Li concentration is due to the ^{6}Li enrichment resulting from the combined effects of migration and isotopic diffusion, both acting in the same direction during discharge. The ^{6}Li enrichment by migration is evidenced by the gain of the ^{6}Li concentration of the electrode, which evolves linearly with the DoD during the CC step rather than with the square root of time (Fick's diffusion law in dilute solution, **Figure S5**). However, isotopic diffusion remains, as the ^{6}Li evolution does not scale directly with the charge passed during the CC and CV steps. At the transition from CC to CV mode (DoD ≈ 84%), only half of the ^{6}Li enrichment measured during the first discharge has already occurred (**Figure S6**). The pronounced increase in ^{6}Li concentration during the CV steps can be attributed to both isotopic diffusion and the homogenization of lithiation across the electrode thickness (linear fit slope within the positive electrode presented in **Figure S7** which correspond to the ^{6}Li gradient). This latter phenomenon is particularly evident in thick, highly loaded electrodes where Li-ion transport is hindered by the morphology and is further amplified in the analyzed region close to the current collector.

During charge (**Figure 4d**), the ^{6}Li transport by migration and isotopic diffusion act in opposite directions. The NMC undergoes delithiation, as evidenced by the overall decrease in ^{6}Li concentration. During the CC step, the ^{6}Li concentration in the positive electrode scales linearly with the SoC (**Figure S5**). Here also, despite the inversion of the directions of the transport phenomena, isotopic diffusion dominates when electrochemical migration is extremely low: indeed, at the end of the CV step (at 97.5 % SoC), where the current has greatly decayed (tenth of the initial value), the ^{6}Li concentration increases slightly in the composite electrode. In order to highlight the ^{6}Li enrichment throughout the cycling, a comparison between the beginning of

first discharge and the end of second charge (**Figure S8**) confirms ^{6}Li transport within the LPSCl matrix and the positive electrode (estimated at 0.31 x10^{21} at/cm^{3}, equivalent to 26.6 % of ^{6}Li enrichment of the positive electrode or corresponding to a global isotopic ratio approx. 10% ^{6}Li - 90% ^{7}Li), although minor contributions from the CEI formation (1.7 % difference in specific capacity from the discharge to the charge) could contribute to this estimation.

3.4.3. Spatially-resolved lithium transport in the separator

Operando neutron imaging (**Movie 1**) further reveals fractures at the separator–electrode interface (highlighted in **Figure 1**) that could locally hinder lithium transport. Such defects, coupled with the intrinsic tortuosity of the composite electrode, exacerbate transport limitations. To spatially resolve these effects, three ^{6}Li concentration profiles in the separator are presented in **Figure 5**.

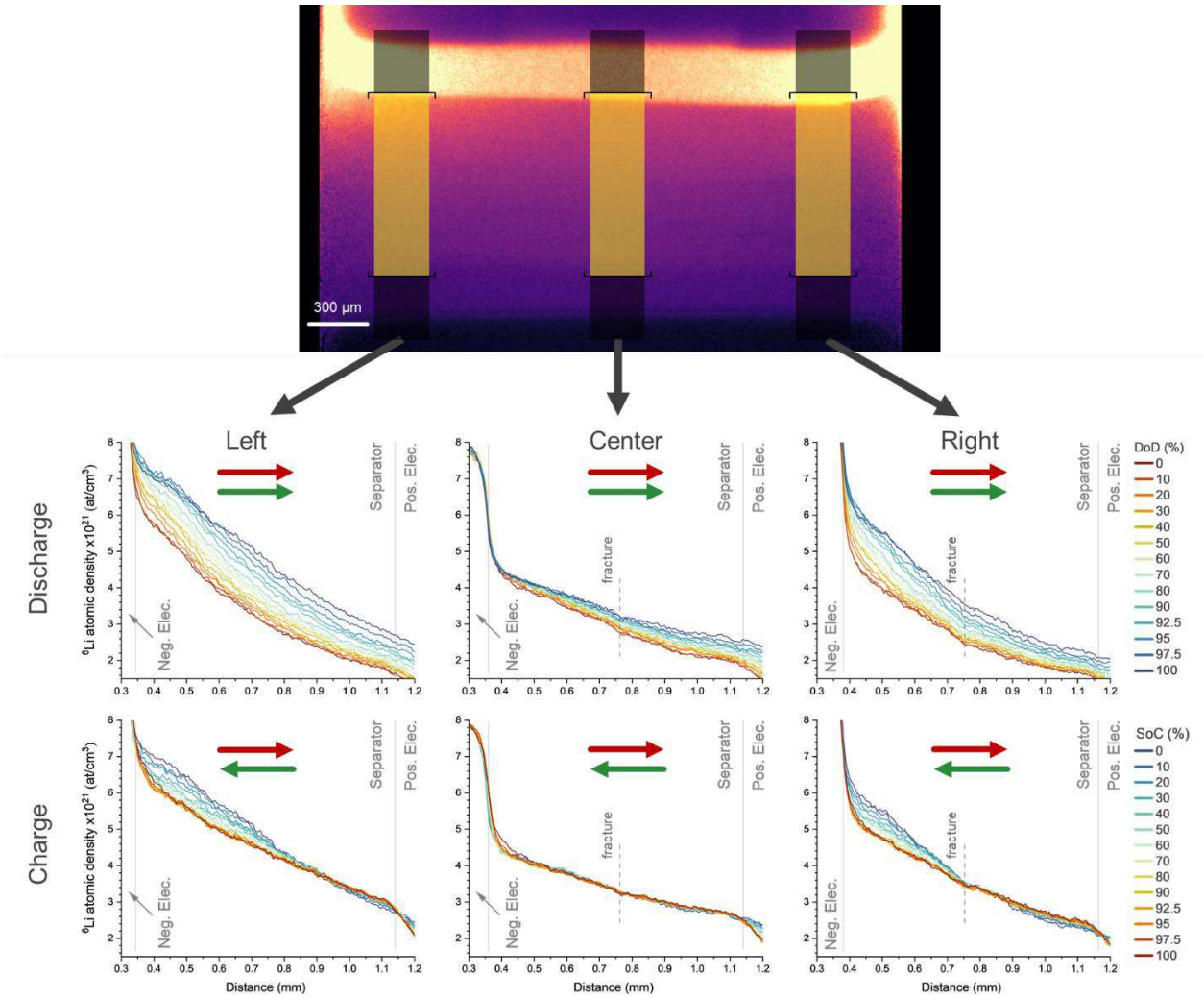


Figure 5: **Spatial evolution of ^{6}Li content during cycling in the separator.** Profiles of lithium content along the separator at different DoD and SoC, averaged over a width of 265 µm. The yellow area between black brackets shows where the profiles were extracted. The red and green arrows highlight the direction of the isotopic diffusion and the electrochemical migration, respectively.

While the behavior of the central profile appears straightforward, edge profiles exhibit a wider range of defects leading to undesired phenomena, including InLi creeping and heterogeneous plating, that complicate their detailed analysis. Spatially resolved ^{6}Li concentration profiles reveal asymmetric transport across the cell width. The radial distribution of porosity has previously been investigated for the same electrolyte and cell architecture at ID19 (ESRF) with

X-Ray Computed Tomography with a voxel size of 1.3 μm (**Figure S9**). This analysis reveals reduced densification at the pellet edge, which results in a higher local porosity compared to the center (**Figure S9c**). While increased porosity at the edges would logically result in lower ^{6}Li concentration, the overall ^{6}Li signal rises throughout the separator during discharge, particularly at the cell edges. These weakly densified regions are the preferential sites where the Li-In alloy could creep in, due to the stack pressure (tens of MPa). Critically, Li-In penetration and plating through the pores alters the local ^{6}Li gradient, thereby enhancing isotopic diffusion at the cell edges. On the right side, fractures induce a marked slope change at 0.75 mm in **Figure 5**, reflecting transport hindrance. Correspondingly, ^{6}Li concentration at the separator–positive electrode interface is greater in the center and left regions than on the fractured right side (approx. 2.7 versus 2.1 x10^{21} at/cm^{3}, respectively).

During charge, the central profile remains stable, whereas the ^{6}Li gradients at the cell edges across the separator progressively diminish, accompanied by a reduction in ^{6}Li concentration at the negative electrode interface. This could be due to the preferential lithium plating at the edges, where higher porosity promotes nucleation[33]. In contrast, the center region already exhibits a flatter ^{6}Li profile, as discussed in the previous section. This is quantitatively supported by the measured ^{6}Li gradient (between 0.45 and 1.1 mm, measured at -1.48 x10^{21} at/cm^{3}·mm in the center) compared to the steeper gradients observed in the left and right edge profiles (-2.03 and -1.88 x10^{21} at/cm^{3}·mm, respectively).

These spatial contrasts underscore the strong coupling between separator microstructure, the subsequent Li-In presence within the separator, and lithium transport dynamics.

3.4.4. Spatially-resolved lithium transport in the composite positive electrode

Three ^{6}Li concentration profiles are plotted in the positive electrode, presented in **Figure 6**:

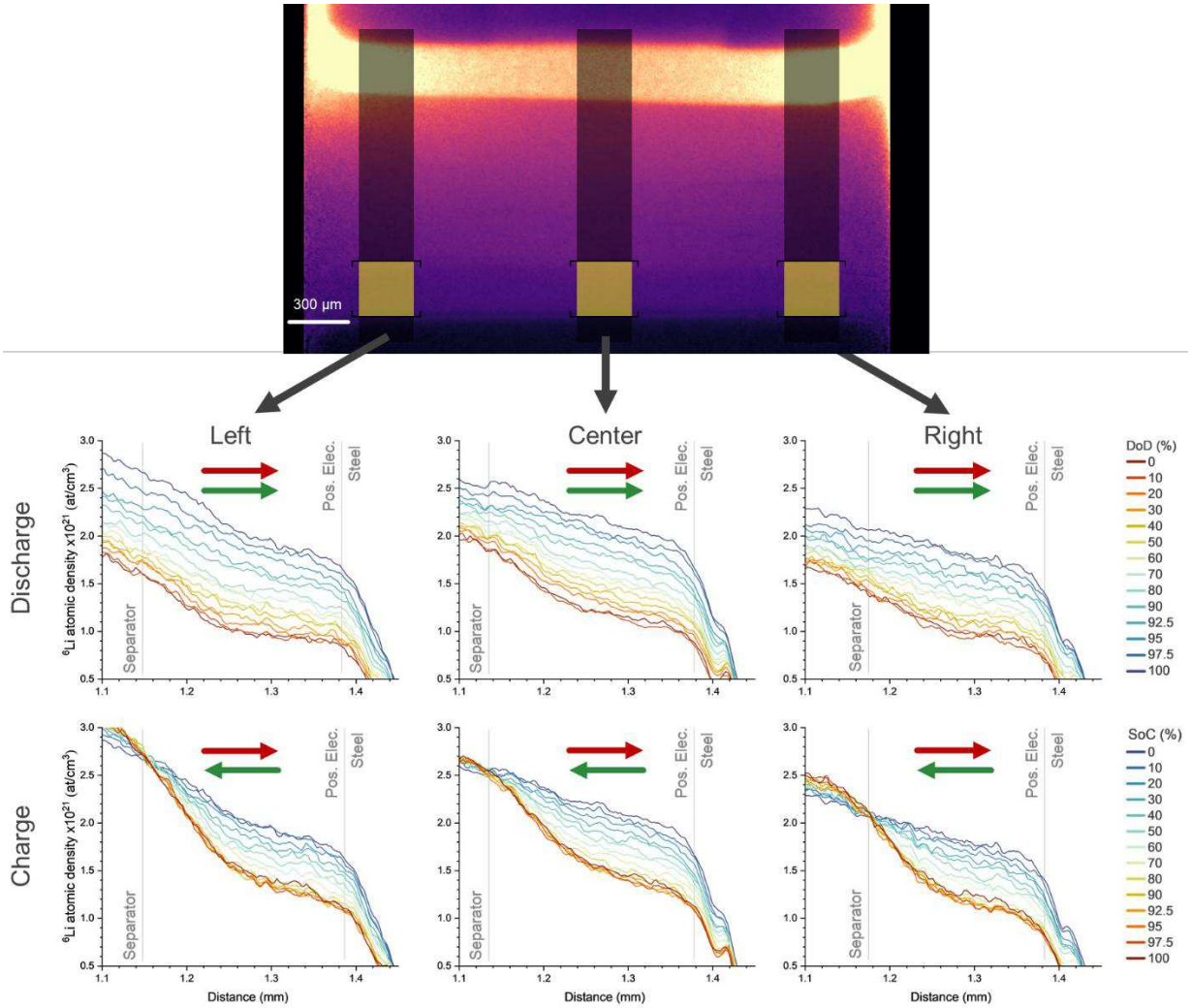


Figure 6: **Spatial evolution of 6Li content during cycling in the positive electrode.** Profiles of lithium content along the positive electrode at different DoD and SoC, averaged over a width of 265 µm. The yellow area between black brackets shows where the profiles were extracted. The red and green arrows highlight the direction of the isotopic diffusion and the electrochemical migration, respectively.

Within the NMC532/LPSCl positive electrode, ^{6}Li enrichment during discharge confirms effective lithiation. As stated previously, the gradient at the separator/positive electrode interface stems from both the tilt of the cell compared to the beam and the rough separator/positive electrode interface; however, trends within the positive electrode can still be extracted after 1.25 mm. Regarding the ^{6}Li concentration at the beginning of the discharge, the lower apparent

^{6}Li concentration at the edges compared to the center (approx. 0.96 x10^{21} versus 1.15 x10^{21} at/cm^{3}, respectively) is consistent with the larger porosity on the edges. During discharge, the increase of ^{6}Li content is the highest in the center, where densification enhances Li transport, both by electrochemical migration (NMC lithiation) and by isotopic diffusion (^{6}Li exchange in LPSCl). In contrast, side regions (particularly the right side) exhibit weaker ^{6}Li evolution due to fractures and higher porosity that disrupt ionic conductivity. More specifically, limited lithiation occurs at the end of the discharge (highlighted by a lower average ^{6}Li atomic concentration of 1.79 x10^{21} vs 2.09 x10^{21} at/cm^{3} in the center), while on the left, where no fracture can be seen, the overall ^{6}Li increase to a significant amount (1.93 x10^{21} at/cm^{3}). The left ^{6}Li concentration is still lower than the center part, mostly due to lower densification.

During charge, delithiation proceeds most efficiently in the dense central zone, while edge regions display slower delithiation, highlighting the strong coupling between electrode microstructure and transport kinetics.

4. Conclusion

High-spatial resolution *operando* radiographies were obtained with a remarkable discretisation (pixel size) of 2.65 µm. The enhanced resolution allowed for a fine investigation of the lithium-ion transport during cycling within the positive electrode and the separator with great detail. By decoupling electrochemical migration from isotopic diffusion, we revealed that both processes concurrently govern the ^{6}Li evolution during cycling, phenomena often overlooked in conventional analyses. Thanks to this approach, we estimated the diffusion coefficient of the ^{6}Li in ^{nat}LPSCl at 2.4 x10^{-6} cm²/s as well as the apparent diffusion flux in different parts of the separator. Despite the inherently 2D nature of neutron radiography, the tailored cell geometry combined with porosity investigation by XCT allowed spatial differentiation between the cell center and its edges, uncovering strong heterogeneities in ionic transport behavior. The denser

region exhibited the most efficient lithium transport, attributed to reduced porosity, fewer fractures, and enhanced ionic percolation. These findings establish a direct link between microstructures, local densification, and lithium mobility, highlighting the necessity of homogeneous electrode microstructure to achieve uniform ionic transport and optimal performance in highly loaded and thick electrodes for solid-state batteries.

5. Methods

Materials

The positive electrode material used in this study, NMC532, was purchased from MSE Supplies. LPSCl was purchased at NEI Corporation, specifying a particle size estimation of 5 µm.

The NMC532 and LPSCl raw powders SEM images are available in Supplementary Information (**Figure S10**).

Cell Assembly

The cell used in this study is a homemade cell[35]. Briefly, the different cell components are shaped using a cell that consists of two stainless steel pressing plungers and a 3 mm PEEK cylinder that provides electrical insulation. For the separator (made only of LPSCl solid electrolyte), roughly 10 mg of ^{nat}LPSCl is added into the cylinder and bottom plunger, then the cell is closed with the top plunger, and a pressure of 410 MPa is applied for 15 min on the powder directly to densify the separator. Then, the cell is opened, and 5.4 mg of the positive composite electrode (CE) mixture is added on one side (the electrode loading was ca. 52.3 mg/cm²). The CE mixture consists of 70% w of ^{nat}NMC523 and 30% w of ^{nat}LPSCl mixed by hand for at least 15 min with a pestle in a mortar. The cell is closed, and the CE is densified alongside the separator at 410 MPa. Lastly, the cell is opened, and a 3 mm electrode of indium lithium is placed as the counter electrode. The indium lithium electrode is made with ^{6}Li to a stoichiometry of $InLi_{0.3}$. The cell is finally closed with the plunger and sealed with an epoxy resin to ensure a moisture-tight cell. Finally, a stack pressure in the MPa range is applied with the dental press.

Electrochemical Cycling

Before the electrochemical measurement performed at the NeXT instrument, the cell was first charged to obtain an electrochemical delithiation of the positive electrode, in particular of the NMC grains (charged at 151 $mAh \cdot g^{-1}$, as presented in **Figure S2**, in accordance with literature[36]). The Galvanostatic cycling with potential limitation (GCPL) method is used to cycle the cell on a VSP300 (Biologic) apparatus directly connected to the cell. The cell has first charged between 2.7 and 4.3 V vs Li^{+}/Li, considering the indium lithium negative electrode potential at 0.62 V vs $Li^{+/}Li$ (between 2.08 and 3.68 V vs $InLi_{0.3}$). A current density corresponding to C/40 is applied. The cell is then stopped and transferred to the instrument to be aligned. Before starting the electrochemical measurement at the instrument, the cell was maintained at a potential of 4.5 V vs Li^{+}/Li before starting the discharge measurement to ensure the cell was properly charged at the beam and to compensate for possible ohmic drops.

Then, the cell has been placed under the beam to follow a full cycle with the same protocol, starting with a discharge (NMC lithiation) from 4.5 to 2.2 V vs Li^{+}/Li and the second charge (NMC delithiation) at a rate of C/20 with a potential hold until the current is a tenth of the initial current. The associated cycling curves are shown in **Figure 1b**.

Neutron Imaging Setup

To ensure an optimal contrast at the neutron imaging instrument, Li isotope must be used. ^{6}Li absorbs approximately fifteen times more neutrons than natural Li ^{nat}Li (78.313 cm^{-1} vs 5.150 cm^{-1} respectively[34]), meaning that a cell made with ^{6}Li with neutron shows high sensitivity, whereas a cell made of ^{nat}Li shows lower sensitivity, where tracking the displacement of Li is more complicated. With ^{nat}Li, the low natural abundance of the ^{6}Li isotope of about 7.4% makes the study of its transport difficult because its contrast is rather negligible. To alleviate this

problem and highlight transport phenomena inside the battery, the negative electrode has been enriched in ^{6}Li while the rest of the cell is at natural isotope abundance.

A specific setup was developed to fulfill the requirement of neutron imaging, generally weakly collimated, to achieve high spatial resolution while ensuring proper electrochemical cycling. Two criteria had to be reached to make this experiment possible: (i) the detector must be as close as possible to the active cell components, and (ii) the cell must exhibit the same electrochemical response as laboratory cell[37]. Both criteria were achieved by using a 3 mm cell developed in the laboratory[35], where the outside frame was replaced by a dental press adapted with 3D printed tough plastic parts to guarantee the stack pressure necessary for the cycling. The press was chosen due to its size and flat profile, perfectly fitting the distance to the detector. The 3D printed parts were designed to fit the press, hold the cell in the same position, and ensure proper electrical connections. The setup is presented in supplementary information in **Figure S1**.

Neutron data acquisition

The measurement has been carried out at Institut Laue-Langevin (ILL, Grenoble, France) at the NeXT instrument. Using an optical magnification of almost 2.5, a spatial discretization (pixel size) of 2.65 µm has been achieved. Considering the pinhole diameter of 15 mm over a collimation distance of 10 m, we were able to distinguish 8 µm wide spokes of a Siemens star resolution target in the sample position. To compensate for the detector's dark current and read-out noise pattern, 33 dark-field images were taken and subtracted from all images. To perform a flat-field correction (reducing non-uniform source contribution/detector response), 33 additional beam reference images are taken without the sample. The cell discharge is then started while 2D neutron radiographs are taken every 10 s.

Neutron image processing

To improve signal-to-noise conditions, 11 flat-field corrected field images are grouped in a stack, and the median value along the stack is taken for each pixel, effectively averaging the signal over these 11 exposures and removing outliers. Due to a slow drift of the cell with respect to the detector during the long *operando* experiment (some tens of μm), all images are registered to the first image by means of an image cross-correlation algorithm.

The natural logarithm of the result images is taken to directly obtain the projected attenuation according to Beer-Lambert's law. Similar to ref. [38], the images are divided by the local sample thickness at each point of the projection to correct for the variable neutron path length in the cylindrical sample of 3 mm diameter. This yields the average value of the linear attenuation coefficient μ along the beam direction for each pixel. For the separator with the formula $^{6}Li_{x}{}^{7}Li_{(6-x)}PS_5Cl$, the linear attenuation coefficient is dominated by absorption (neutron capture) and varies linearly with the number x of ^{6}Li atoms replacing a ^{7}Li atom. We used the formula $\mu(x)=(0.084+5.035x)$/cm derived from the NIST scattering database, assuming a mass density of 1.5 g/cm^3. Inversion of this linear dependency yields us directly the substitution number x and thus the atomic density (atoms/unit volume) for the ^{6}Li species.

References

1. Janek, J. & Zeier, W. G. Challenges in speeding up solid-state battery development. *Nat. Energy* **8**, 230–240 (2023).
2. Zheng, F., Kotobuki, M., Song, S., Lai, M. O. & Lu, L. Review on solid electrolytes for all-solid-state lithium-ion batteries. *J. Power Sources* **389**, 198–213 (2018).
3. Li, C. *et al.* An advance review of solid-state battery: Challenges, progress and prospects. *Sustain. Mater. Technol.* **29**, e00297 (2021).
4. Xu, C., Chen, L. & Wu, F. Unveiling the power of sulfide solid electrolytes for next-generation all-solid-state lithium batteries. *Mater.* **6**, 100428 (2025).
5. Kodama, M., Ohashi, A. & Hirai, S. In situ X-ray computational tomography measurement of single particle behavior of sulfide solid electrolyte under high-pressure compression. *J. Power Sources Adv.* **4**, 100019 (2020).
6. Tsukasaki, H., Mori, S., Shiotani, S. & Yamamura, H. Ionic conductivity and crystallization process in the Li2S–P2S5 glass electrolyte. *Solid State Ion.* **317**, 122–126 (2018).
7. Boulineau, S., Courty, M., Tarascon, J.-M. & Viallet, V. Mechanochemical synthesis of Li-argyrodite Li6PS5X (X=Cl, Br, I) as sulfur-based solid electrolytes for all solid state batteries application. *Solid State Ion.* **221**, 1–5 (2012).
8. Wang, S. *et al.* High-Conductivity Argyrodite Li6PS5Cl Solid Electrolytes Prepared via Optimized Sintering Processes for All-Solid-State Lithium–Sulfur Batteries. *ACS Appl. Mater. Interfaces* **10**, 42279–42285 (2018).
9. Choi, W. *et al.* Formulating Interfacial Impedances for Designing High-Energy and High-Power All-Solid-State Battery Cathodes. *ACS Appl. Mater. Interfaces* **16**, 26066–26078 (2024).
10. Albertus, P. *et al.* Challenges for and Pathways toward Li-Metal-Based All-Solid-State Batteries. *ACS Energy Lett.* **6**, 1399–1404 (2021).

11. Kato, Y. *et al.* All-Solid-State Batteries with Thick Electrode Configurations. *J. Phys. Chem. Lett.* **9**, 607–613 (2018).
12. Neumann, A. *et al.* Analysis of Interfacial Effects in All-Solid-State Batteries with Thiophosphate Solid Electrolytes. *ACS Appl. Mater. Interfaces* **12**, 9277–9291 (2020).
13. Kalnaus, S., Dudney, N. J., Westover, A. S., Herbert, E. & Hackney, S. Solid-state batteries: The critical role of mechanics. *Science* **381**, eabg5998 (2023).
14. Perrenot, P., Bayle-Guillemaud, P. & Villevieille, C. Composite Electrode (LiNi0.6Mn0.2Co0.2O2) Engineering for Thiophosphate Solid-State Batteries: Morphological Evolution and Electrochemical Properties. *ACS Energy Lett.* 4957–4965 (2023) doi:10.1021/acsenergylett.3c01975.
15. Zhang, J. *et al.* Deformation and fracture mechanisms in the calendering process of lithium-ion battery electrodes. *Appl. Energy* **373**, 123900 (2024).
16. Yan, Z., Wang, L., Zhang, H. & He, X. Determination and Engineering of Li-Ion Tortuosity in Electrode Toward High Performance of Li-Ion Batteries. *Adv. Energy Mater.* **14**, 2303206 (2024).
17. Hlushkou, D. *et al.* The influence of void space on ion transport in a composite cathode for all-solid-state batteries. *J. Power Sources* **396**, 363–370 (2018).
18. Minnmann, P. *et al.* Editors' Choice—Visualizing the Impact of the Composite Cathode Microstructure and Porosity on Solid-State Battery Performance. *J. Electrochem. Soc.* **171**, 060514 (2024).
19. Morino, Y. Degradation rate at the Solid–Solid interface of sulfide-based solid Electrolyte–Cathode active material. *J. Power Sources* **541**, 231672 (2022).
20. Renais, C. *et al.* Understanding Fast Charging Ability Limitation in Graphite Electrode for Li-Ion Batteries: Quasi-Thermodynamic Approach and Methodology. *Chem. Mater.* https://doi.org/10.1021/acs.chemmater.5c00722 (2025) doi:10.1021/acs.chemmater.5c00722.
21. Perrenot, P. *et al.* Room-Temperature Sintering of Amorphous Thiophosphate Solid Electrolyte (Li3PS4): Coupling Morphological Evolution to Electrochemical Properties. *Adv. Funct. Mater.* **n/a**, 2310739 (2023).

22. Meyer, T. *et al.* Isotopic Labeling: A Powerful Tool to Investigate Lithium Transport in a Polymer-Ceramic Composite Electrolyte Designed for Solid-State Batteries. *ACS Appl. Energy Mater.* **7**, 9939–9952 (2024).
23. Davis, A. L. *et al.* Rate Limitations in Composite Solid-State Battery Electrodes: Revealing Heterogeneity with Operando Microscopy. *ACS Energy Lett.* **6**, 2993–3003 (2021).
24. Stavola, A. M. *et al.* Lithiation Gradients and Tortuosity Factors in Thick NMC111-Argyrodite Solid-State Cathodes. *ACS Energy Lett.* **8**, 1273–1280 (2023).
25. Ziesche, R. F. *et al.* 4D imaging of lithium-batteries using correlative neutron and X-ray tomography with a virtual unrolling technique. *Nat. Commun.* **11**, 777 (2020).
26. Lanz, M., Lehmann, E., Imhof, R., Exnar, I. & Novák, P. In situ neutron radiography of lithium-ion batteries during charge/discharge cycling. *J. Power Sources* **101**, 177–181 (2001).
27. Siegel, J. B. *et al.* Neutron Imaging of Lithium Concentration in LFP Pouch Cell Battery. *J. Electrochem. Soc.* **158**, A523 (2011).
28. Zhou, H. *et al.* Probing Multiscale Transport and Inhomogeneity in a Lithium-Ion Pouch Cell Using In Situ Neutron Methods. *ACS Energy Lett.* **1**, 981–986 (2016).
29. Xu, C. *et al.* Operando Neutron Imaging of Lithium Flux and Gradient Cathode Design for Enhanced Kinetics in High-Loading All-Solid-State Li─S Batteries. *Adv. Mater.* **38**, e11553 (2026).
30. Bradbury, R. *et al.* Visualizing Reaction Fronts and Transport Limitations in Solid-State Li–S Batteries via Operando Neutron Imaging. *Adv. Energy Mater.* **13**, 2203426 (2023).
31. Ji, T. *et al.* Operando neutron imaging-guided gradient design of Li-ion solid conductor for high-mass-loading cathodes. *Nat. Commun.* **16**, 7667 (2025).
32. de Klerk, N. J. J., Rosłoń, I. & Wagemaker, M. Diffusion Mechanism of Li Argyrodite Solid Electrolytes for Li-Ion Batteries and Prediction of Optimized Halogen Doping: The Effect of Li Vacancies, Halogens, and Halogen Disorder. *Chem. Mater.* **28**, 7955–7963 (2016).

33. Tambio, S. J. *et al.* Self-diffusion of electrolyte species in model battery electrodes using Magic Angle Spinning and Pulsed Field Gradient Nuclear Magnetic Resonance. *J. Power Sources* **362**, 315–322 (2017).
34. Bradbury, R. *et al.* Visualizing Lithium Ion Transport in Solid-State Li–S Batteries Using 6Li Contrast Enhanced Neutron Imaging. *Adv. Funct. Mater.* **33**, 2302619 (2023).
35. Wu, X. *et al.* Operando Visualization of Morphological Dynamics in All-Solid-State Batteries. *Adv. Energy Mater.* **9**, 1901547 (2019).
36. Wang, C. *et al.* Single crystal cathodes enabling high-performance all-solid-state lithium-ion batteries. *Energy Storage Mater.* **30**, 98–103 (2020).
37. Wu, X., El Kazzi, M. & Villevieille, C. Surface and morphological investigation of the electrode/electrolyte properties in an all-solid-state battery using a Li2S-P2S5 solid electrolyte. *J. Electroceramics* **38**, 207–214 (2017).
38. Cordonnier, B. *et al.* Neutron Imaging of Cadmium Sorption and Transport in Porous Rocks. *Front. Earth Sci.* **7**, (2019).
39. Schindelin, J. *et al.* Fiji: an open-source platform for biological-image analysis. *Nat. Methods* **9**, 676–682 (2012).
40. Meyer, T., Gutel, T., Manzanarez, H., Bardet, M. & De Vito, E. Lithium Self-Diffusion in a Polymer Electrolyte for Solid-State Batteries: ToF-SIMS/ssNMR Correlative Characterization and Modeling Based on Lithium Isotopic Labeling. *ACS Appl. Mater. Interfaces* **15**, 44268–44279 (2023).
41. Lodding, A., Mundy, J. N. & Ott, A. Isotope Inter-Diffusion and Self-Diffusion in Solid Lithium Metal. *Phys. Status Solidi B* **38**, 559–569 (1970).

Acknowledgement

The authors would like to thank Dr. Sergio F. Mayer for his 3D printing frame. The authors would also like to thank Dr. Thomas Meyer for his insights and for the valuable discussion on lithium isotope diffusion. Special acknowledgments are made to open software Fiji and its incredible developers.

Competing interests

The authors declare no competing interests.

Figure and table legends

Figure 1: **Operando neutron radiography and electrochemical profile of a solid-state cell after initial charge.** a) Neutron radiography highlighting the different cell components obtained after the first charge. The gradient of color (big arrow), as well as the fractures (dashed lines) in the separator, are highlighted. The arrow represents the gradient in the direction of the spontaneous isotopic diffusion of ^{6}Li from high concentration in orange to low concentration in violet, and b) Electrochemical profile of the cell cycled in CCCV (Constant Current Constant Voltage) mode at a C/20 rate between 4.5 and 2.2 V vs Li^{+}/Li at the NeXT instrument. 7

Figure 2: ***Operando*** **neutron radiography of ^{6}Li redistribution during cycling at key states of discharge and charge.** a) Neutron radiography images at DoD 0 % (left), at DoD 100 %, equivalent to SoC 100 % (center), and at SoC 100 % (right), and b) their associated ^{6}Li concentration profiles that highlight the evolution of Li-ion concentration during cycling. 9

Figure 3: **Simulated ^{6}Li atomic density profiles at key stages** (based on calculation from cell fabrication without electrochemical migration): a) initial cell assembly, b) intermediate diffusion,

and c) infinite diffusion time, illustrating the interplay of isotopic diffusion and electrochemical migration (red and green arrows, respectively) during d) assembly, e) charge, and f) discharge. 11

Figure 4: **Evolution of ^{6}Li content during cycling at the center of the cell.** Profiles of ^{6}Li content along the cell components at different DoD and SoC during a, c) discharge and b, d) charge, averaged over a width of 265 µm in the center of the cell. The top panels focus on the separator, and the bottom panels focus on the positive electrode, respectively. The red and green arrows highlight the direction of the isotopic diffusion and the electrochemical migration, respectively. The dashed line indicates the position of an identified fracture. The arrows on the right help visualize the curves' evolution during cycling. 14

Figure 5: **Spatial evolution of ^{6}Li content during cycling in the separator.** Profiles of lithium content along the separator at different DoD and SoC, averaged over a width of 265 µm. The yellow area between black brackets shows where the profiles were extracted. The red and green arrows highlight the direction of the isotopic diffusion and the electrochemical migration, respectively. 19

Figure 6: **Spatial evolution of 6Li content during cycling in the positive electrode.** Profiles of lithium content along the positive electrode at different DoD and SoC, averaged over a width of 265 µm. The yellow area between black brackets shows where the profiles were extracted. The red and green arrows highlight the direction of the isotopic diffusion and the electrochemical migration, respectively..... 21

Table 1: Concentration calculation at the initial state t_0 and at infinite time. The bold values are the ones presented in **Figure 3**..... 11

Figure S1: Pictures of the experimental setup at NeXT instrument in a) the same direction of the beam and b) a side view. c) the 3D printed frame that it fixed in the modified dental press, which allowed high spatial resolution neutron radiography imaging. 37

Figure S2: First charge of the cell (NMC532 vs. $In^6Li_{0.3}$, with LPSCl as a solid electrolyte) cycled at a C/40 rate and 25°C in the laboratory between 2.5 to 4.3 V vs Li^+/Li. 37

Figure S3: Measurement of the projected area (highlighted in yellow) of the positive electrode by image analysis at the charged state. 39

Figure S4:Profiles of ^6Li content along the cell components at different DoD and SoC during a, c) discharge and b, d) charge, averaged over the entire width of the sample. The top panels focus on the separator and the bottom panels focus on the positive electrode, respectively. The red and green arrows highlight the direction of the isotopic diffusion and the electrochemical migration, respectively. The dashed line indicates the position of an identified fracture. The arrows on the right help visualize the curves' evolution during cycling. 44

Figure S5: ^6Li atomic density as function of a) DoD and SoC and b) the square root of time at various height in the separator and in the positive electrode, measured in the center over a width of 265 µm, highlighting diffusion-driven transport. The red and green arrows refer to the direction of the isotopic diffusion and the electrochemical migration, respectively. These concepts are further explained in “Isotopic diffusion vs. electrochemical migration”. 45

Figure S6: Profiles of lithium content along the cell components at different DoD, averaged over the width of the sample, with the highlight of the switch from galvanostatic to potentiostatic regime (at DoD 84%). 46

Figure S7: Slope of the linear fit in the positive electrode of the ^{6}Li atomic density in function of the DoD, extracted from **Figure 4** and **Figure S4**. 47

Figure S8: ^{6}Li profiles of lithium content at different DoD and SoC, averaged over the width of the sample, highlighting the evolution of ^{6}Li due to isotopic diffusion in the separator and the positive electrode as the cell come back to its original state of SoC 100%. 48

Figure S9: Spatial distribution measurement of porosity made at ID19 (ESRF) on LPSCl separator. a) the integrated radial distribution of porosity, highlighting higher porosity on the edge of the sample. b) the height-wise distribution per slice of porosity, showing homogeneous porosity along the height of the separator. c) 3D representation of the porosity in the LPSCl separator with the pellet diameter of 3 mm with the arrows in the center showing the radial integration and the arrow on the side showing the height-wise measurement. 49

Figure S10: Secondary electrons images of a), c), e) the LPSCl powder and b), d), f) the NMC532 powder..... 50

Table S1: Concentration calculation of the pristine state of the composite electrode (CE), the separator, and the negative electrode. 39

Table S2: Concentration calculation at the delithiated state of the composite electrode. 41

Table S3: Concentration calculation at the relithiated state of the composite electrode. 42

Table S4: Diffusion coefficient calculation based on the equivalent electrochemical migration. 43

Supplementary Files

This is a list of supplementary files associated with this preprint. Click to download.

- 02SupplementaryInfoOperandoneutronradiography.pdf
- Operandoneutronradiographysourcedata.xlsx
- Movie16Liatomicdensity.mp4